

**1 Size-differentiated Export Flux in Different Dynamical  
2 Regimes in the Ocean**

**3 M. Dever<sup>1</sup>, D. Nicholson<sup>1</sup>, M. M. Omand<sup>2</sup>, and A. Mahadevan<sup>1</sup>**

**4** <sup>1</sup>Woods Hole Oceanographic Institution, Woods Hole, MA 02543, USA

**5** <sup>2</sup>Graduate School of Oceanography, University of Rhode Island, Narragansett, Rhode Island, USA

**6 Key Points:**

- 7** • Submesoscale dynamics enhance the contribution of slow-sinking particles to  
**8** POC export, especially for steep particle size-spectrum slopes  
**9** • Remineralization processes intensify the role of slow-sinking particles, to the  
**10** point where these particle sometime dominate POC export

11 **Abstract**

12 Export of Particulate Organic Carbon (POC) is mainly driven by gravitational sinking.  
 13 Thus, traditionally, it is thought that larger, faster-sinking particles make up  
 14 most of the POC export flux. However, this need not be the case for particles whose  
 15 sinking speeds are comparable to the vertical velocities of a dynamic flow field that can  
 16 influence the descent rate of particles. Particles with different settling speeds are re-  
 17 leased in two process-oriented model simulations of an upper ocean eddying flow in the  
 18 Northeast Pacific to evaluate the impact of (1) ocean dynamics on the respective con-  
 19 tribution of the different sinking-velocity classes to POC export, and (2) the particle  
 20 number size-spectrum slope. The analysis reveals that the leading export mechanism  
 21 changes from gravitationally-driven to advectively-driven as submesoscale dynamics  
 22 become more active in the region. The vertical velocity associated with submesoscale  
 23 dynamics enhances the contribution of slower-sinking particles to POC export flux  
 24 by a factor ranging from 3 to 10, especially where the relative abundance of small  
 25 particles is large, (i.e., steep particle size-spectrum slope). Remineralization generally  
 26 decreases the total amount of biomass exported, but its impact is weaker in dynamical  
 27 regimes where submesoscale dynamics are present and export is advectively-driven.  
 28 In an advectively-driven export regime, remineralization processes counter-intuitively  
 29 enhance the role of slower-sinking particles to the point where these slower-sinking ve-  
 30 locity classes dominate the export, therefore challenging the traditional paradigm for  
 31 POC export. This study demonstrates that slow-sinking particles can be a significant  
 32 contribution, and at times, even dominate the export flux.

33 **1 Introduction**

34 Photosynthesis in the sunlit upper ocean and the production of Particulate Or-  
 35 ganic Carbon (POC) takes up dissolved inorganic carbon and facilitates the uptake of  
 36 CO<sub>2</sub> from the atmosphere. The sinking of POC exports organic carbon from the upper  
 37 ocean to the interior, leading to the sequestration of carbon (Falkowski et al., 1998;  
 38 Boyd et al., 2019) on timescales ranging from days to years depending on the sink-  
 39 ing depth and circulation. Despite progress on sampling and viewing particles in the  
 40 ocean, direct measurements of particles sinking velocities are difficult to obtain, and  
 41 often inferred from key parameters such as particle type, size, and density (McDonnell  
 42 & Buesseler, 2010; McDonnell & Buesseler, 2012).

43 Traditionally, POC export is thought to occur through gravitational sinking and  
 44 one-dimensional models have been used to describe the sinking POC flux with depth  
 45 (Jackson et al., 1997; Armstrong et al., 2001; DeVries et al., 2014; Omand et al.,  
 46 2020). Particles produced through primary and secondary production in the surface  
 47 layer that are relatively large and fast sinking tend to sink out of the upper surface  
 48 layer on timescales shorter than the timescale on which the particles get remineralized.  
 49 It is reasonable to treat POC export as sinking-dominated if the vertical advective  
 50 velocities in the ocean are weaker than the velocities associated with gravitational  
 51 sinking. However, Particulate Organic Matter (POM) has a wide range of particle  
 52 shape, size and type, that result in particle sinking velocities ranging from practically  
 53 zero, to several hundreds of meters per day (Riley et al., 2012; Baker et al., 2017).  
 54 The size spectrum, or number distribution of particle sizes, is usually characterized by  
 55 a power law with the power ranging between -2 and -4, for which the abundance of  
 56 small particles is  $\mathcal{O}(10^4 - 10^8)$  greater than large particles (McCave, 1984; Petrik et  
 57 al., 2013). The biomass size spectrum, which indicates the distribution of biomass vs.  
 58 particle size, tends to be flatter and variable in shape (Sheldon et al., 1972) compared  
 59 to the particle number spectrum, because the volume (and mass) of a particle scales  
 60 with its linear size raised to a power that exceeds 1 (and typically varies between 2  
 61 and 3 depending on shape and porosity). Importantly, it means that a significant  
 62 fraction of the particulate biomass is in the small size fraction (Richardson & Jackson,

63 Even though the sinking velocity  $w_s$  of particles does not perfectly relate to  
 64 particle size  $l$ , it is fair to assume that  $w_s \sim l^n$  (with  $n = 2$  according to Stokes law,  
 65 and  $1 < n < 2$  for complex particle shapes). Due to this, as well as the fact that  
 66 particles of organic matter are not very much greater in their densities than seawater,  
 67 a significant fraction of the biomass sinks very slowly (at velocities less than tens of  
 68 meters per day). When the gravitational sinking velocity of particles is comparable  
 69 to (or smaller than) the vertical velocities in the flow field, the dynamics of the flow  
 70 field can impact the trajectories and fate of the POC. Thus, depending on the flow  
 71 dynamics, and the fraction of slow-sinking particulate biomass, the sinking of organic  
 72 matter can be affected by the fluid flow in the ocean.

73 Recent studies have shown that ocean dynamics can play a role in driving the  
 74 transport of carbon from the euphotic layer to the ocean interior (Stukel & Ducklow,  
 75 2017; Stukel et al., 2018; Llort et al., 2018). For example, enhanced vertical velocities  
 76 along the edge of a mesoscale eddy led to a funneling of particles along the eddy's  
 77 periphery (van Haren et al., 2006; Waite et al., 2016) and in mesoscale features in the  
 78 California current (Stukel et al., 2017). Omand et al. (2015) found that submesoscale  
 79 mixed layer eddies, while contributing to the restratification of a frontal zone, were  
 80 subducting a large amount of non-sinking POC from the surface productive layer  
 81 during the onset of the Spring bloom in the subpolar North Atlantic. Advectively  
 82 subducting plumes or filaments of high oxygen, chlorophyll and small POC (evidenced  
 83 through backscatter) were detected from a suite of gliders during the North Atlantic  
 84 Bloom experiment (Alkire et al., 2012). Using model simulations to capture the process  
 85 of eddy-driven subduction, Omand et al. (2015) estimated the downward advective  
 86 flux of non-sinking POC and parameterized it. Briggs et al. (2011) quantified the  
 87 flux of fast-sinking particles consisting largely of diatoms from observations of optical  
 88 backscatter. But, these estimates did not account for a range of sinking particle  
 89 velocities. Typically, POM has a wide spectrum of sinking velocities and in order  
 90 to understand its fate and export, we need to consider the biomass distribution as a  
 91 function of the particle sinking velocity spectrum and its interaction with the dynamics  
 92 of the flow field in the ocean.

93 A growing body of literature focusing on submesoscale (1-10 km) dynamics is ex-  
 94 ploring its impact on biogeochemical processes (Lévy et al., 2012; Mahadevan, 2016).  
 95 Submesoscale dynamics, characterized by Rossby numbers of order 1, typically develop  
 96 in filaments in areas where sharp density fronts exist (Thomas, Taylor, et al., 2013;  
 97 Klein & Lapeyre, 2009; McWilliams, 2016). In this dynamical regime, geostrophic bal-  
 98 ance breaks down and a secondary ageostrophic circulation develops across the front,  
 99 capable of generating large vertical velocities on the order of 100 m/day (Fox-Kemper  
 100 et al., 2008; Mahadevan, 2016). On the denser side of the front, the vorticity is cyclonic  
 101 and associated with downwelling velocities, while anticyclonic vorticity and upwelling  
 102 is expected on the lighter side of the front. The distribution of relative vorticity as-  
 103 sociated with submesoscale dynamics near the surface exhibits an asymmetry with  
 104 higher values of positive vorticity than negative vorticity (Rudnick, 2001), leading to  
 105 more localized and more intense downwelling regions, as opposed to weaker and larger  
 106 scale upwelling regions (Mahadevan & Tandon, 2006). Enhanced vertical velocities  
 107 can aid the supply nutrients to the sunlit layer of the ocean for primary production  
 108 (Mahadevan & Archer, 2000; Lévy et al., 2001) or can significantly increase the ex-  
 109 port of POC to the ocean interior through localized downwelling (Lévy et al., 2012;  
 110 Gruber et al., 2011; Estapa et al., 2015; Omand et al., 2015), a process that might not  
 111 be captured if submesoscales O(1 km) are not fully resolved (Resplandy et al., 2019).  
 112 The downwelling velocities  $\mathcal{O}(100 \text{ m/day})$  generated at submeso-scales provide a phys-  
 113 ical mechanism for exporting slow sinking or neutrally buoyant particles on timescales  
 114 shorter than their remineralization timescales. If the fraction of biomass associated  
 115 with such slow sinking velocities is significant, submesoscale dynamics can potentially  
 116 impact the export of POC.

We rely on a submesoscale-resolving, non-hydrostatic ocean model to simulate the dynamics in the upper few hundred meters of the ocean. The dynamical model is coupled with a particle-tracking module to model the advection of particles by fluid flow, while neglecting the effects of particle inertia and drag on their advection. In addition, the particles sink with a range of sinking velocities (between 0.025–5 m day<sup>-1</sup>) that is based on the range of vertical currents modeled in this region. We aim to address the transitional regime of the particle sinking velocity spectrum, where both advection and sinking speeds have similar order of magnitudes. A similar study with sinking tracers showed the influence of the flow (Taylor et al., 2020), but the use of particles enables a characterization of export associated with each sinking class of particles.

The model is used to quantify the contribution of slow-sinking particles to carbon export, as a function of (1) the dynamics of the flow field, (2) the slope of the sinking velocity spectrum, and (3) the remineralization timescale. Particles in the model are prescribed with both a constant and time-varying sinking velocity to mimic a remineralizing behavior. Particles are released in two fundamentally different flow fields in terms of dynamics based on observed conditions in the Northeast Pacific: In the summer, where ocean dynamics are characterized by low Rossby numbers and weak vertical advective velocities, and in the winter, where ocean dynamics include submesoscale frontal structures and local Rossby numbers  $\mathcal{O}(1)$ . Both simulations and the particle-tracking module are described in Section 2. The impact of particles characteristics and ocean dynamics on the export of POC is quantified in Section 3, and discussed in Section 4. Section 5 summarizes the key conclusions of the study.

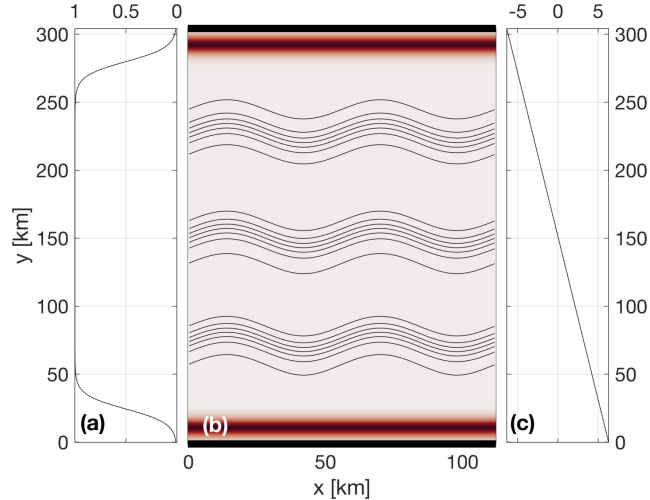
## 2 Methods

### 2.1 Model setup and domain

This study uses a non-hydrostatic, three-dimensional, Process Study Ocean Model (PSOM; Mahadevan et al., 1996b, 1996a) to simulate an eddy field that is representative of the Northeast Pacific Ocean. The model is set in a channel configuration with periodic east-west boundaries, and solid boundaries in the south and north. The domain covers 112 km in the x-direction, 304 km in the y-direction, and 1000 m in the vertical (Figure 1). The horizontal resolution is 500 m, while a stretched grid is used in the vertical with 32 levels ranging in thickness from 1.25 m near the surface to 70 m at the lowermost level. The model is integrated numerically in time and evolves the temperature, salinity, free-surface height, pressure, and three-dimensional velocity field from an initial state, subject to momentum and buoyancy fluxes applied through the surface boundary.

Time-varying wind stress and heat flux are prescribed at the surface boundary. Time series are computed from measurements collected at Station Papa and available through the Pacific Marine Environmental Laboratory (PMEL, 2018). Daily wind stress and net heat fluxes are calculated over the period 2007-2016 to produce a year-long climatology. A squared low-pass filter with a cut-off frequency of 8.5 days is applied to both time series to remove high-frequency variability. In all numerical experiments, simulations are run for the first 5 days without any forcing applied to the surface boundary. Surface wind stress and heat fluxes are then linearly ramped up between days 5 and 10 of the simulation, to reach realistic values at day 10.

While the meridional component,  $\tau_y$ , is set to zero, the zonal component of the wind stress,  $\tau_x$ , is prescribed at the surface throughout the model domain and is tapered at the northern and southern boundaries to avoid excessive Ekman-driven upwelling and downwelling (Figure 1a). A restoration timescale is prescribed to contain the curl-driven upwelling and downwelling regions generated by the tapering of the



153 **Figure 1.** PSOM model setup. (a) Meridional profile of scaling coefficient that multiplies the  
 154 time-varying zonal wind stress  $\tau_x$  shown in Fig. 3a. The taper at north and south boundaries  
 155 prevents ‘coastal’ up-/down-welling being entirely concentrated in the boundary grid cell. (b)  
 156 Restoration factor (color shading) used to dampen internal wave reflection at boundaries as well  
 157 as up-/down-welling due to the windstress curl. Surface density contours (black) show the three  
 158 fronts used to initialize the model. (c) Meridional variation of the time-dependent surface heat  
 159 flux (Fig. 3a) prescribed over the domain.

174 wind stress, as well as to limit internal wave reflection at the solid boundaries back  
 175 into the domain (Figure 1b). While net surface heat fluxes are homogeneous in the  
 176 zonal direction, a meridional gradient is maintained throughout the simulation. The  
 177 meridional gradient was determined from the North American Regional Reanalysis  
 178 (NARR) product (Mesinger et al., 2006), and set to  $1/24 \text{ W/m}^2/\text{km}$  (Figure 1c).

179 Initial hydrographic conditions are determined from a three-dimensional gridded  
 180 field of temperature and salinity from Argo floats (Gaillard, 2015; Gaillard et al., 2016).  
 181 Argo data is averaged monthly over the period 2002-2012 and two different months are  
 182 used to initialize the two main numerical experiments for this study: Climatological  
 183 conditions in April are used to initialize the *Papa-summer* experiment, while January  
 184 climatological conditions are used to initialize the *Papa-winter* experiment (Table 1).  
 185 The north-south background density gradient is then intensified into three fronts lo-  
 186 cated at  $y = 75$ ,  $y = 150$ , and  $y = 225$  km (Figure 1). The amplitude of the density  
 187 gradient associated with the three fronts is determined from the probability distri-  
 188 bution function (PDF) of the density gradients measured by underwater gliders deployed  
 189 around Station Papa over the period 2008-2010 (Pelland et al., 2016; Pelland, 2018).  
 190 To reduce model spin-up time, density fronts are perturbed by a sinusoidal wave with  
 191 a wavelength close to the 1st baroclinic deformation radius ( $\lambda = 66$  km). Similar  
 192 PSOM configurations were successfully used in previous studies (Mahadevan et al.,  
 193 2012; Omand et al., 2015). The model does not simulate surface waves or boundary  
 194 layer turbulence, but rather, examines the fate of particulate organic matter beneath  
 195 the turbulent surface boundary layer.

196 Two main experiments are conducted using the same configuration of PSOM,  
 197 where only initial conditions and surface forcings are varied: *Papa-summer* aims at  
 198 generating ocean dynamics representing conditions in the Northeast Pacific in the sum-  
 199 mertime. Summer ocean dynamics are characterized by a flow generally in geostrophic

220      **Table 1.** Summary of the key characteristics of PSOM experiments *Papa-summer* and  
 221      *Papa-winter*.

	<i>Papa-summer</i>	<i>Papa-winter</i>
Time period	April – July	January – March
Spin-up	60 days	50 days
Advective timestep	216 s	108 s
Horizontal diffusivity	$1 \text{ m}^2 \text{ s}^{-1}$	$0.2 \text{ m}^2 \text{ s}^{-1}$
Restoration timescale	3 days	15 days
Zonal wind stress	$0 - +0.16 \text{ N m}^{-2}$	$-0.05 - +0.17 \text{ N m}^{-2}$
Surface heat flux	$-46.8 - +167.5 \text{ W m}^{-2}$	$-57.6 - +15.3 \text{ W m}^{-2}$
Maximum $M^2 (\times 10^{-8})$		
initial	$3.2 \text{ s}^{-2}$	$33.9 \text{ s}^{-2}$
spun-up	$12.0 \text{ s}^{-2}$	$50.0 \text{ s}^{-2}$
Maximum $N^2 (\times 10^{-4})$		
initial	$1.5 \text{ s}^{-2}$	$1.6 \text{ s}^{-2}$
spun-up	$3.1 \text{ s}^{-2}$	$1.1 \text{ s}^{-2}$
Averaged mixed layer depth		
initial	73 m	85 m
spun-up	11 m	93 m

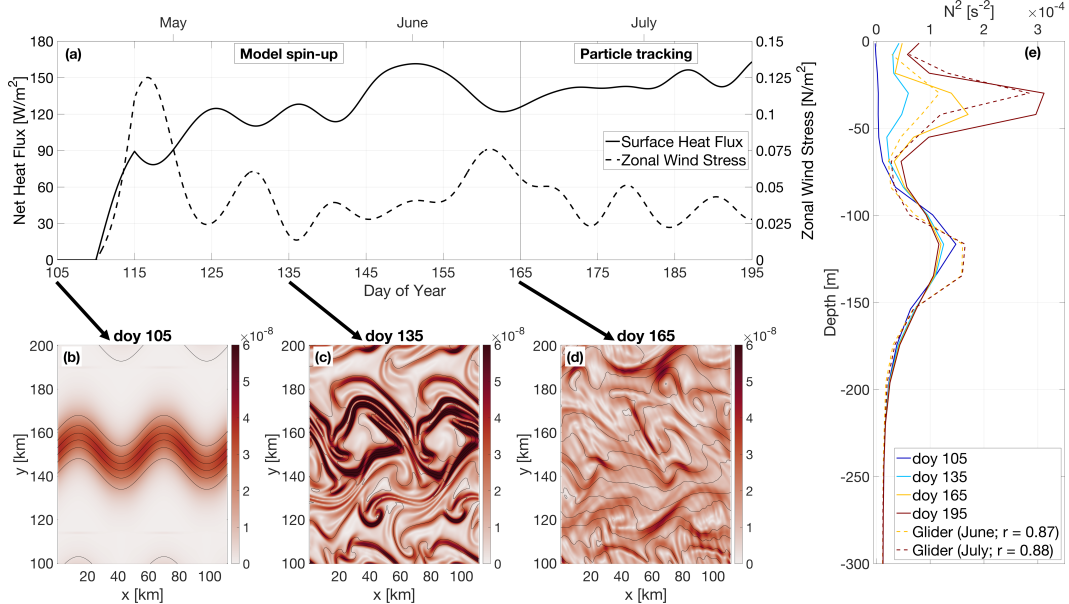
200      balance, with relatively weak density gradients and low Rossby numbers ( $Ro \ll 1$ ).  
 201      *Papa-winter* aims at capturing wintertime ocean conditions in the region. A different  
 202      dynamical regime is expected to dominate during wintertime when mixed layers are  
 203      deeper and lateral density gradients enhanced, with sharper density fronts, filament-  
 204      like features and localized Rossby number  $Ro = \mathcal{O}(1)$  over spatial scales  $\mathcal{O}(1 \text{ km})$   
 205      (Mensa et al., 2013; Callies et al., 2015; Thompson et al., 2016). The individual  
 206      characteristics of each of *Papa-summer* and *Papa-winter* are detailed below.

### 207      2.1.1 *Papa-summer Model Experiment*

208      In *Papa-summer*, PSOM is initialized based on climatological Argo data in April.  
 209      The magnitude of the density gradient across the front is set to  $3.34 \times 10^{-6} \text{ kg/m}^3/\text{m}$ ,  
 210      which corresponds to the 95<sup>th</sup> percentile of the PDF of density gradients measured  
 211      in April from glider data collected in the region (Figure 2 and Table 1). The model  
 212      is run with a timestep of 216 s and is allowed to spin-up for 60 days, allowing sum-  
 213      mer stratification to develop. The model is then run for 30 additional days, saving  
 214      instantaneous model fields every 3 hours for particle tracking. The month of April  
 215      is chosen for initialization so the experiment would capture the onset of positive net  
 216      heat fluxes, and the summer restratification that ensues in July-August (Figure 2). In  
 217      this region, the summer stratification is associated with large primary productivity,  
 218      particle production, and POC export (e.g., fecal pellets, dead phytoplankton; Plant  
 219      et al., 2016).

### 231      2.1.2 *Papa-winter Model Experiment*

232      In *Papa-winter*, PSOM is initialized based on climatological Argo data in Jan-  
 233      uary. The frontal gradient is set to  $3.54 \times 10^{-5} \text{ kg/m}^3/\text{m}$ , which corresponds to the  
 234      99<sup>th</sup> percentile of the PDF of density gradients measured in January from glider data  
 235      collected in the region (Figure 3 and Table 1). The model is allowed to spin-up for 50  
 236      days allowing for the prescribed fronts to become unstable. To accommodate for the  
 237      larger density gradients and stronger velocities, the advective timestep is shortened to

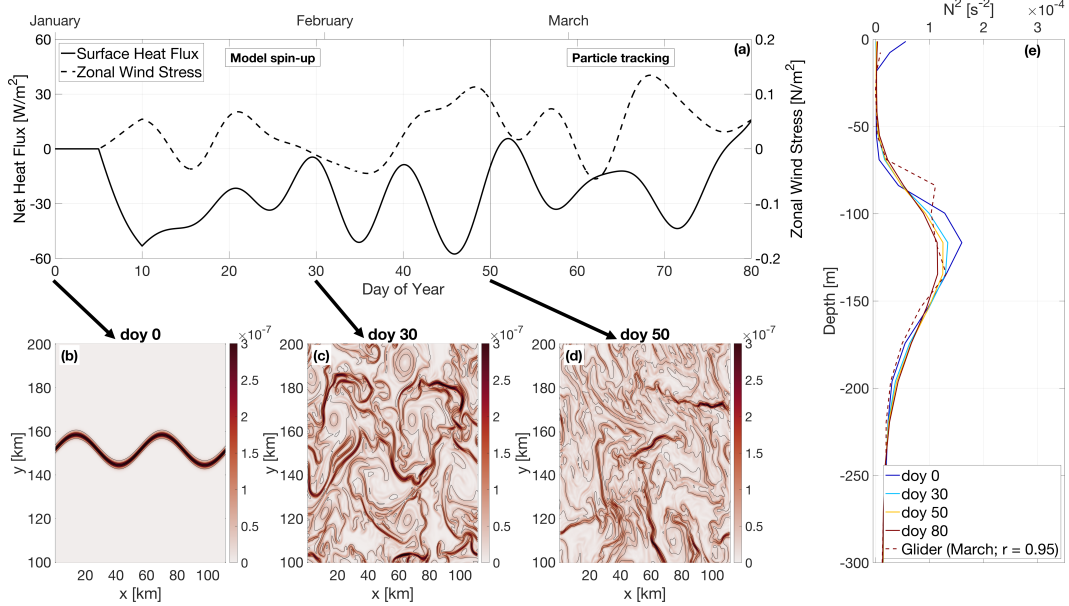


222 **Figure 2.** PSOM configuration for *Papa\_summer*. (a) Time series of net heat fluxes and wind  
 223 stress prescribed at the surface. Notice the positive heat fluxes, as well as downfront winds (i.e.  
 224 eastward) persisting throughout the experiment. (b)-(d) surface horizontal buoyancy gradients  
 225  $M^2 = |\nabla_H b|^2$  (in  $s^{-2}$ ) at day of year (doy) 105, 135, and 165. Black contours show isopycnals (in  
 226 kg/m<sup>3</sup>; CI = 0.01 kg/m<sup>3</sup>). (e) Vertical profile of the buoyancy frequency  $N^2$  at day of year 105,  
 227 135, 165, and 195, showing the development of summer stratification centered at  $z = 30$  m (solid  
 228 lines). Monthly-average vertical stratification obtained from glider profiles collected in June and  
 229 July are superimposed (dashed lines), along with the correlation coefficient between observations  
 230 and model outputs.

238 108 s and the horizontal diffusivity is lowered to 0.2 m<sup>2</sup>/s throughout the experiment.  
 239 The model is run for 30 additional days, saving instantaneous model fields every 1.5  
 240 hours for particle tracking. The month of January is chosen for initialization so the  
 241 experiment would capture the time of year where the mixed layer is the deepest, and  
 242 Rossby number O(1) occur more frequently. The objective is for this experiment to  
 243 contrast *Papa\_summer* by capturing the statistics of ocean conditions dominated by  
 244 submesoscale dynamics.

### 253 2.1.3 Validation

254 To ensure that PSOM simulations yielded realistic conditions for both *Papa\_summer*  
 255 and *Papa\_winter*, distributions of horizontal ( $M^2$ ) and vertical ( $N^2$ ) buoyancy gradi-  
 256 ents are compared with glider observations collected over the period 2008-2009 (Pelland  
 257 et al., 2016). During this period, underwater gliders sampled in a “bow-tie” pattern  
 258 centered on Station Papa. Gliders sample the water column in a triangular wave  
 259 pattern, whose shape is easily affected by currents, due to the slow moving speed of  
 260 the glider (~1 km/hr). It is therefore challenging to associate a specific spatial scale  
 261 with gradients computed between glider profiles, as profile separation distances can be  
 262 highly variable through depth and time. To circumvent this issue, horizontal buo-  
 263 nyancy gradients are computed between each pair of glider profiles available within one  
 264 branch of the bow-tie. Each along-track lateral buoyancy gradient is thus associated  
 265 with a specific separation scale and a timestamp. Glider-based density gradients can



245 **Figure 3.** PSOM configuration for *Papa\_winter*. (a) time series of net heat fluxes and wind  
 246 stress prescribed at the surface. Notice the mostly negative heat fluxes, as well as alternating  
 247 zonal wind direction. (b)-(d) surface horizontal buoyancy gradients  $M^2 = |\nabla_H b|^2$  (in  $s^{-2}$ ) at day  
 248 of year (doy) 0, 30, and 50. Black contours show isopycnals (in  $kg/m^3$ ; CI = 0.01  $kg/m^3$ ). (e)  
 249 Vertical profile of the buoyancy frequency  $N^2$  at doy 0, 30, 50, and 80, showing the persistence  
 250 of the halocline between  $z = 80$  and  $z = 180$  m throughout the experiment (solid lines). Monthly-  
 251 average vertical stratification obtained from glider profiles collected in March is superimposed  
 252 (dashed line), along with the correlation coefficient between observations and model outputs.

266 be affected by internal waves. To filter the impact of internal waves on the PDF of  
 267 horizontal buoyancy gradients, only gradients computed at a scale of twice the Rossby  
 268 radius  $\pm 1$  km are considered. Rossby radii are estimated from the glider data and  
 269 are  $\sim 8$  km in winter and  $\sim 20$  km in summer.

## 270 2.2 Particle Tracking Experiments

### 271 2.2.1 Particle Advection Scheme

To quantify the impact of submesoscale dynamics on the export of Particulate Organic Matter (POC), Lagrangian particle trajectories are computed using the same scheme as in “TRACMASS” (Döös et al., 2013) with the flow fields from the two experiments described above. The three-dimensional, non-divergent velocity components from the faces of each “C” grid cell are linearly interpolated onto the particle’s position within the grid cell. For example, the eastward (along the x-axis) velocity of a particle is given by

$$u(x) = u_{i-1} + \frac{(x - x_{i-1})}{(x_i - x_{i-1})}(u_i - u_{i-1}), \quad (1)$$

where the subscripts  $i - 1$  and  $i$  denote the western and eastern walls of the grid cell where the particle is located, respectively. This can be re-written as

$$\frac{\partial x}{\partial t} + \beta x + \delta = 0, \quad (2)$$

where  $\beta = (u_i - u_{i-1})/\Delta x$  and  $\delta = -u_{i-1} - \beta x_{i-1}$  (Döös et al., 2013). This differential equation can be solved analytically for  $\beta \neq 0$  as

$$x_{t_1} = \left( x_0 + \frac{\delta}{\beta} \right) \exp^{-\beta(t_1-t_0)} - \frac{\delta}{\beta} \quad (3)$$

The time it will take for the particle to reach the eastern or western face of the grid cell can be computed by taking  $x_{t_1} = x_i$  or  $x_{t_1} = x_{i-1}$ , respectively, and solving for  $t_1$ . For each advective timestep, the times required for the particle to reach any of the 6 walls of the grid cell are computed using (3). If any of those times is shorter than the advective timestep, the particle is advected until it reaches the cell wall. Then the flow field in the adjacent grid cell is considered and the particle is advected over the remaining time.

### 2.2.2 Particle Seeding

For all particle-tracking experiments, a single particle seeding event is prescribed. In the horizontal, particles are seeded every 250 m over the entire domain in the x-direction, and for  $100 < y < 200$  km in the y-direction. The seeding is centered over the mean position of the central front (see Figure 2) and is therefore not affected by undesired effects created by the solid north-south solid boundaries. In the vertical, particles are seeded every 1 m between 75 and 85 m. This depth range is chosen as it corresponds to the average euphotic depth at Station Papa, defined by the 1% light level. Particle seeding is located at the base of the euphotic layer where biological processes not captured by the particles (e.g., grazing, repackaging, aggregation, etc.) are not as active (Ducklow et al., 2001). The euphotic depth was computed for the months of February and June over the period 2007-2016 from profiles of Photosynthetically Active Radiation (PAR) collected at Station Papa as part of the long-term monitoring of Line P executed by the Department of Fisheries and Ocean Canada<sup>1</sup>. The average euphotic depth computed for both of these months is around 80 m, which agrees with previously established estimates of the euphotic depth (Sherry et al., 1999; Harrison et al., 2004).

In each particle-tracking experiment, three different classes of particles are released. Each particle class is characterized by a different sinking velocity: 0.025, 1, and 5 m/day. In this study, these particle classes are referred to as slow-, intermediate-, and fast-sinking particles. This characterization is not based on the absolute value of the sinking rate, but rather on the ratio with vertical currents in the study region. The slowest-sinking class is essentially selected to represent non-sinking particles: based on the setup of our experiments, the slowest-sinking particles would take 400 days to sink 10 m through gravitational sinking, a timescale much greater than commonly observed remineralization timescales. While 5 m/day remains a relatively slow sinking rate, this “fastest-sinking” velocity is chosen as an end-member velocity class of particle, based on the PDF of vertical velocities in the model. At any given time, at least 85% of the model vertical velocity is weaker than 5 m/day. The results presented for the 5 m/day sinking class can therefore be theoretically extrapolated to any class with a higher sinking velocity.

The advective timestep for particles is set to 1.5 hours. The flow field is linearly interpolated in time between model outputs, justifying the higher temporal resolution used for particle tracking in *Papa\_winter*. Particle positions are saved every 3 hours, along with key model variables interpolated onto the particle positions (e.g., density, vorticity). Particles are tracked for four weeks (28 days). Each particle-tracking experiment contains 1,971,717 particles per sinking-velocity class, for a total of 9,858,585 particles.

<sup>1</sup> <https://www.waterproperties.ca/linep/index.php>

### 317 2.2.3 Density and Biomass Spectra

To quantify vertical export fluxes, both the distribution of the number of particles and the associated biomass can be modeled based on two main variables: the particles' radii and the rate at which the number of particles changes with respect to the size. The particle number is modeled using a power-law function as a function of size that is driven by the parameter  $\xi$ . This slope  $\xi$  of the size spectrum of particles (also known as the Junge slope; White et al., 2015) is the slope of the log-log curve of particle number  $N$  vs. particle radius  $r$ , where

$$N(r) = N_0 \left( \frac{r}{r_0} \right)^{-\xi}. \quad (4)$$

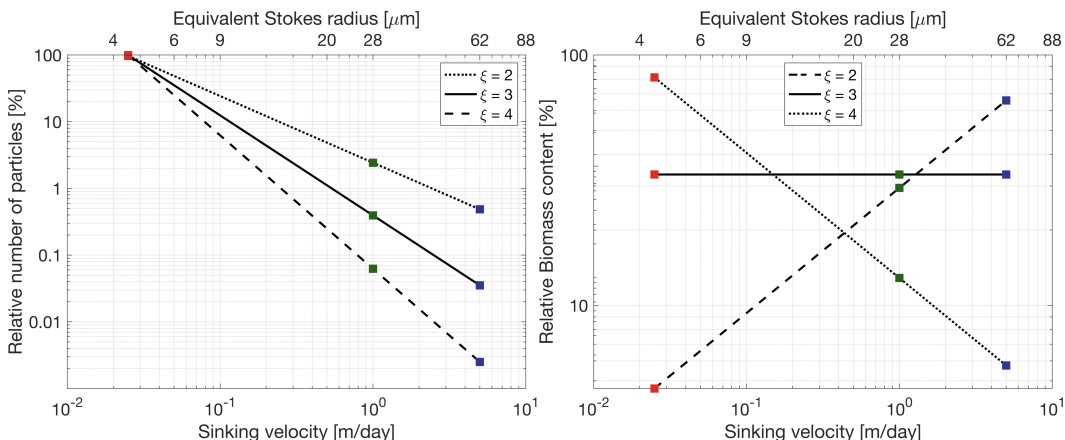
318 Here,  $N_0$  and  $r_0$  represent a reference particle number and radius, chosen arbitrarily.  
 319 Typical values for  $\xi$  derived from both in-situ observations and satellite data have been  
 320 reported to range from 3 to 6 (Kostadinov et al., 2009; White et al., 2015). For small  
 321 particles ( $<400 \mu\text{m}$ ) and relatively low temperature ( $<15^\circ\text{C}$ ), it has been shown that  
 322 the relationship between particle radius  $r$  and sinking velocity  $w_s$  exhibits a range of  
 323 variation and is difficult to determine empirically. Nevertheless, Stokes' law, where  
 324  $w_s \propto r^2$ , is often used as a lower-bound sinking velocity estimate (Bach et al., 2012).

Assuming a Stokes-like relationship, we can construct based on (4) a particle sinking velocity spectrum  $N(w_s)$ , as a function of the Junge slope  $\xi$ :

$$N(w_s) = N_0 \left( \frac{w_s}{w_{s_0}} \right)^{-\xi/2}, \quad (5)$$

325 where  $w_{s_0}$  is the sinking speed of particles with radius  $r_0$ . For a specific slope and  
 326 sinking-velocity class, an equivalent number of particles per simulated particle can be  
 327 computed using (5) (See Figure 4). For example, using the largest sinking velocity  
 328 class as a reference (i.e.,  $w_{s_0} = 5 \text{ m/day}$  and  $N_0 = 1,971,717$ ), and a spectral slope  
 329  $\xi = 4$ , each simulated particle with a sinking velocity of  $0.025 \text{ m/day}$  in fact represents  
 330 40,000 particles (Figure 4).

The relative biomass of a particle in a specific sinking-velocity class,  $B_p(w_s)$  can be estimated if the biomass is assumed to scale with the particle's volume. The relative biomass of one particle in a sinking-velocity class  $w_s$  can therefore be computed as



331 **Figure 4.** Relative number of particles (left) and biomass (right) as a function of sinking  
 332 velocity  $w_s$ . Sinking velocity spectrum are shown for three different Junge slope  $\xi$ : 2 (dotted),  
 333 3 (solid), and 2 (dashed). Colored squares indicate the sinking velocities of the three particle  
 334 classes modeled: 0.025 m/day (red), 1 m/day (green), and 5 m/day (blue).

$$B_p(w_s) = B_p(w_{s_0}) \left( \frac{w_s}{w_{s_0}} \right)^{3/2} \quad (6)$$

where  $B_p(w_{s_0})$  is the biomass of a particle in the sinking velocity class  $w_{s_0}$ . The total biomass associated with one simulated particle can be obtained by scaling (6) by the ratio  $N(w_s)/N_0$ :

$$B(w_s) = B_0 \left( \frac{w_s}{w_{s_0}} \right)^{3/2} \frac{N(w_s)}{N_0} \quad (7)$$

where  $B_0 = B_p(w_{s_0})$ . Combining (5) and (7) yields an expression relating the biomass associated with a simulated particle for a specific sinking-velocity class and the spectral slope (Figure 4):

$$B(w_s) = B_0 \left( \frac{w_s}{w_{s_0}} \right)^{\frac{3-\xi}{2}}. \quad (8)$$

Using the same example as before where  $\xi = 4$ , if the amount of biomass associated with one simulated particle in the 5 m/day sinking-velocity class is taken as  $B_0 = 1$ , then one simulated particle sinking at 0.025 m/day contains 14.14 units of biomass and a single particle contains  $14.14/40,000 = 3.5 \times 10^{-4}$  units of biomass (see Figure 4). This normalized formulation of particle number and biomass (see Equations (5) and (8)) has the advantage that the impact of spectral slope on the relative export of biomass can be quantified without needing a large number of particle-tracking experiments, where the number of seeded particles would vary to account for the different spectral slopes. For the purpose of this study, only the relative amount of biomass is relevant. For simplicity, we define a normalized biomass unit for  $\xi = 3$  as  $B_0 = 1$ . The values taken by  $B_0$  for other Junge slopes  $\xi$  are computed under the condition that the total amount of biomass is kept constant (Figure 4b).

#### 2.2.4 Particle Remineralization Scheme

Remineralization of particles as they sink through the water column impacts the amount of biomass exported. Slow-sinking particles generally contain less biomass and spend more time in the mixed layer, which means that they are remineralized at a shallower depth than faster sinking particles. Remineralization processes are complex, species-dependent, and generally not well-understood. In the absence of a consensus on a general functional form of particle remineralization, we rely on an idealized relationship which assumes that the biomass content of a particle decreases in time proportionally to the particle volume. Remineralization is thus modeled as an exponential decrease of biomass with time at a rate  $k$  (Iversen & Ploug, 2010, 2013)

$$B(t) = B^0 \exp(-kt), \quad (9)$$

where  $B^0$  denotes the biomass content at  $t = 0$  days, and the remineralization rate is taken to be  $k = 0.13 \text{ day}^{-1}$  in this study (Iversen & Ploug, 2010). This remineralization rate is independent of particle sinking velocity, and seems to lie within the range of other estimates (Ploug et al., 2008; Iversen & Ploug, 2010, 2013). The change in biomass with time is in turn expected to affect the sinking velocity of the particle. Given that  $B \propto w^{3/2}$  (see Equation (6)), particles in all sinking-velocity classes undergo a decay in sinking speed according to

$$w_s(t) = w_s^0 \exp\left(-\frac{2kt}{3}\right), \quad (10)$$

where  $w_s^0$  is the initial sinking velocity at  $t = 0$  days. In this study, the impact of remineralization is thus considered through the implementation of a time-dependent sinking velocity (Equation 10). While particles classes are classified based on their initial sinking-velocity, it is worth noting that over the length of the particle-tracking experiments that include remineralization (28 days), particle sinking speeds slow down to 10% of their initial velocity.

354 **3 Results**

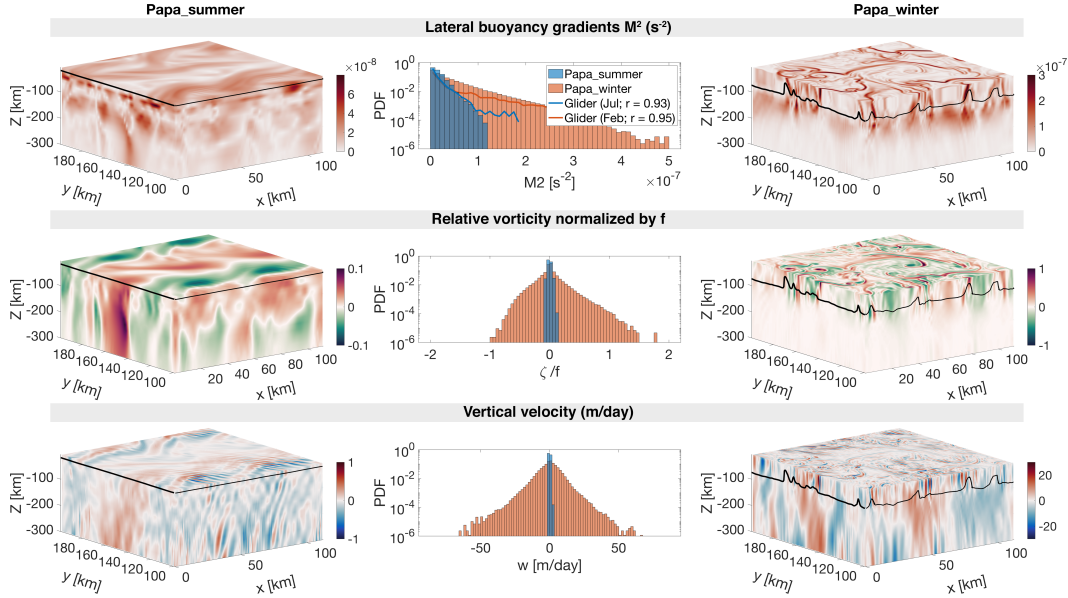
355 **3.1 Seasonally varying dynamical regimes**

356 Two model experiments are designed to capture different dynamical conditions  
 357 observed in the Northeast Pacific Ocean in summer and winter. *Papa\_summer* is ini-  
 358 tialized in early spring (doy 105) when the water column is characterized by a relatively  
 359 deep mixed layer ( $\sim 100$  m) and a halocline located between 100 and 150 m (Figure  
 360 2). The forcing by a realistic, positive, net heat flux generates the restratification of  
 361 the water column, with the development of a strong thermocline between 25 and 50 m  
 362 leading to the shoaling of the mixed layer and a subsurface peak in  $N^2$  at about 30 m  
 363 (see Figure 2). A comparison between model outputs and monthly-averaged density  
 364 profiles from underwater gliders collected in June and July over the period 2008-2009  
 365 yields correlation coefficients of  $r = 0.87$  and  $r = 0.88$ , respectively. These high cor-  
 366 relation suggest that *Papa\_summer* numerical experiment captures the vertical spring  
 367 and summer conditions in the Northeast Pacific Ocean.

368 In the horizontal, the prescribed density fronts progressively become unstable  
 369 within the first 60 days of the experiment (Figure 2). During this time, the Total  
 370 Kinetic Energy ( $KE_{tot}$ ) contained in the model domain slowly increases before reach-  
 371 ing a maximum at doy 162, where it remains relatively constant for the rest of the  
 372 simulation. The flattening of the  $KE_{tot}$  curve is used to determine the time necessary  
 373 for the simulation to spin-up, hence determining the start day of the particle-tracking  
 374 experiments. The ocean dynamics associated with *Papa\_summer* are characterized  
 375 using PDFs of horizontal buoyancy gradients ( $M^2 = |\nabla_H b|^2$ ), vertical velocities ( $w$ ),  
 376 and Rossby numbers computed from the normalized vertical component of the relative  
 377 vorticity ( $Ro = (v_x - u_y)/f$  where  $f = 1.12 \times 10^{-4}$ ; Figure 5).

385 Lateral buoyancy gradients in the summer are relatively weak  $\mathcal{O}(10^{-8} \text{ s}^{-2})$  and  
 386 result in low Rossby numbers  $\mathcal{O}(0.1)$ , with positive relative vorticity on the denser  
 387 (north) side of the front and negative relative vorticity on the lighter (south) side  
 388 of the front. Corresponding vertical velocities are consistently weaker than 1 m/day  
 389 ( $< 10^{-5} \text{ m/s}$ ) and are characterized by regions of weak upwelling and downwelling on  
 390 10 km scales, associated with the meandering of the front (Bower & Rossby, 1989).  
 391 Alternating bands of upwelling and downwelling at  $\mathcal{O}(1 \text{ km})$  spatial scale are super-  
 392 imposed, and likely caused by propagating internal waves. Coherent vertical velocities  
 393 structures extend to depths much greater than the mixed layer depth ( $\sim 25$  m; Figure  
 394 5). The amplitude of the vertical velocity field coincides with the expected order of  
 395 magnitude given by the scaling  $w \propto Ro f U / N$  (Mahadevan, 2016): using  $Ro \sim 0.1$   
 396 (Figure 5),  $N \sim 10^{-2} \text{ s}^{-1}$  (Figure 2),  $f \sim 10^{-5} \text{ s}^{-1}$ , and  $U \sim 0.01 \text{ m/s}$ , we obtain  
 397  $w \sim 10^{-6} \text{ m/s}$ , or  $\sim 10^{-1} \text{ m/day}$ .

398 *Papa\_winter* is, on the other hand, initialized in the winter (doy 0) to capture a  
 399 time period where the mixed layer depth is deeper ( $\sim 100$  m) and density gradients  
 400 more pronounced (Pelland et al., 2016). At this time of year, the water column in  
 401 this region is characterized by the presence of a deep halocline between 100 and 150  
 402 m (Figure 3 Pelland et al., 2016). After spin-up, the vertical stratification remains  
 403 consistent throughout the model run, and compares well with the vertical profile ob-  
 404 tained from glider observations for the month of March ( $r = 0.95$ ; see Figure 3). In  
 405 the horizontal, prescribed density fronts are much sharper than in summer (i.e., over  
 406 smaller spatial scales  $\mathcal{O}(1 \text{ km})$  vs.  $\mathcal{O}(10 \text{ km})$ ). Because of these stronger density  
 407 gradients, combined with the alternating zonal winds and constantly negative surface  
 408 heat flux, the fronts become unstable more rapidly than in summer (Figure 3). As a  
 409 result,  $KE_{tot}$  starts to plateau at doy 48. The experiment is considered spun-up by  
 410 doy 50 and the particle-tracking experiment is initialized.



378 **Figure 5.** Snapshots of  $M^2$  (top),  $\zeta/f$  (middle), and  $w$  (bottom) half-way through the  
 379 particle tracking experiment for *Papa\_summer* (left) and *Papa\_winter* (right), with the Mixed Layer  
 380 Depth indicated by the solid black line. The corresponding Probability Distribution Functions  
 381 (PDFs) are shown in the center for both *Papa\_summer* (blue) and *Papa\_winter* (red). Note the  
 382 different colorbars used for *Papa\_summer* and *Papa\_winter*. Histograms of  $M^2$  computed from  
 383 glider data at Station Papa in February (blue line) and July (red line) are superimposed in the  
 384 top middle panel.

411 The frontal structures visible in the horizontal buoyancy gradient field are as-  
 412 sociated with filaments of relatively high Rossby number of  $\mathcal{O}(1)$  (Figure 5). The  
 413 PDF of relative vorticity reveals a positively-skewed distribution ( $s = 0.68$ ). This is in  
 414 agreement with the fact that the relative vorticity is more likely to be cyclonic than  
 415 anticyclonic, based on conservation of potential vorticity (Hoskins & Bretherton, 1972).  
 416 Regions with high Rossby number are localized and located in the mixed layer exclu-  
 417 sively. In places where the local Rossby number reaches  $\mathcal{O}(1)$ , geostrophic balance is  
 418 lost and a vertical secondary ageostrophic circulation begins to slump the isopycnals  
 419 and restore the flow to a more geostrophically-balanced flow. This ageostrophic sec-  
 420 ondary circulation therefore generates “hot spots” of higher vertical velocities. The  
 421 fine-scale structures in the vertical velocity field corresponding to  $\mathcal{O}(1)$  Rossby num-  
 422 bers can be seen in Figure 5, with local vertical velocities up to 60 m/day ( $\sim 7 \times 10^{-4}$   
 423 m/s). Contrary to the PDF of relative vorticity ( $s = -0.25$ ). This is in agreement with the theory:  
 424 In fact, positive relative vorticity is associated with the dense side of a density front,  
 425 where vertical velocities are negative (Mahadevan, 2016). Once again, the amplitude  
 426 of these vertical velocity hot spots is coherent with the scaling  $w \propto RofU/N$ : using  
 427  $Ro \sim 1$ ,  $N \sim 10^{-2}$  1/s,  $f \sim 10^{-5}$  1/s, and  $U \sim 0.1$  m/s, we obtain  $w \sim 10^{-4}$  m/s, or  
 428  $\sim 10^1$  m/day.

430 Comparing *Papa\_summer* and *Papa\_winter* highlights the different dynamical  
 431 regimes in the two experiments. In *Papa\_winter*, density fronts tend to be sharper,  
 432 meaning larger density gradients over shorter spatial scales. When computed at the  
 433 kilometer-scale, the PDF of horizontal buoyancy gradients in *Papa\_winter* exhibits a  
 434 longer tail than in *Papa\_summer* (Figure 5). When compared to observations, the

435 PDFs of  $M^2$  in *Papa-summer* and *Papa-winter* demonstrate a correlation with obser-  
436 vations of  $r = 0.93$  and  $r = 0.95$ , respectively.

437 The wider PDF of vertical velocities in *Papa-winter* shows advective velocities  
438 that match and exceed typical gravitational sinking velocities, particularly for smaller,  
439 and therefore slower-sinking, particulate organic material. The secondary ageostrophic  
440 circulation that develops at submeso-scales (i.e.,  $\text{Ro} \sim O(1)$ ) therefore generates an ex-  
441 port mechanism that directly competes with the traditional paradigm that relies on  
442 gravitational sinking leading the export of particulate matter in the ocean.

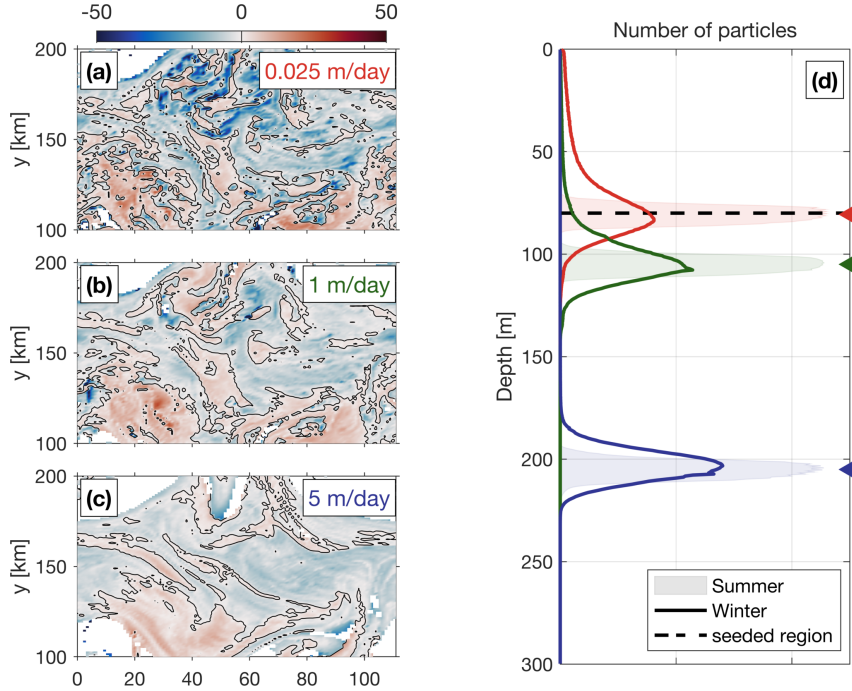
### 443 3.2 Gravitational and Advective Export of POC

444 Both model experiments described above were then used to investigate the re-  
445 lationship between ocean dynamics and particle downward flux, using Lagrangian  
446 particle-tracking. Domain-averaged, downward particle flux is expected to be a com-  
447 bination of the flux driving by gravitational sinking ( $\langle w_s B \rangle$ ), and by the vertical ad-  
448 vective currents affecting the particle along its pathway ( $\langle wB \rangle$ ). The deviation in  
449 particle depths from the traditional one-dimensional gravitationally driven model is  
450 shown in Figure 6 for both summer and winter cases. In the summer, the PDF of par-  
451 ticle density versus depth remains relatively narrow through time, and is centered on  
452 a depth level that can be predicted using a simple 1D gravitational model (see shaded  
453 curves in Figure 6). The spread in the particle density also vary little among particle  
454 classes with different sinking velocities, suggesting that downward fluxes of particles  
455 is greatly dominated by gravitational settling and is not subject to significant vertical  
456 ocean currents.

468 In the winter, however, PDFs of particle density versus depth is wider, in agree-  
469 ment with the stronger vertical ocean currents occurring in the winter (see Figure 5).  
470 A top-view of the deviation in the downward particle flux from the traditionally con-  
471 sidered 1D gravitational model can be seen in Figure 6 (panels (a)-(c)). Slower-sinking  
472 particles deviate more than faster-sinking particles, exhibiting median depth anom-  
473 alies up to 50 m. This is due to the fact that slower-sinking particles spend more time  
474 in the mixed layer, where most of the stronger vertical currents tend to occur (Figure  
475 5). An interesting result emerges from the spatial distribution of the depth-anomaly:  
476 both positive (i.e., particles are shallower than expected) and negative (i.e., particles  
477 are deeper than expected) anomalies are organized into features with a length-scale  
478  $O(1\text{-}10 \text{ km})$ . This further highlights the importance of winter submesoscale circulation  
479 for vertical fluxes of particles.

480 A relative amount of biomass is associated to the particles using Equation (8).  
481 PDFs of relative biomass as a function of the vertical velocity is shown in Figure 7.  
482 Following the traditional paradigm derived from the simple 1D gravitational model, the  
483 downward flux of biomass in the summer is dominated by faster-sinking particle classes  
484 capable of carrying particulate material downwards more efficiently. The contribution  
485 of slower-sinking particles, however, depends critically on the slope of the size spectrum  
486 (see Figure 4). As the Junge slope increases, the spectrum of biomass steepens, and  
487 the relative contribution of slower-sinking particles to the downward biomass flux  
488 significantly increases (Figure 7c). In fact, the contribution of slower-sinking particles  
489 to the summer downward flux increases by a factor 100 (from 0.2% to 20%) when the  
490 Junge slope varies from  $\xi = 2$  to  $\xi = 4$ . While significant, the impact of a change in  
491 the Junge slope in summer conditions does not challenge the dominant role played by  
492 faster-sinking particles. This result can be explained by the fact that, in the summer,  
493 vertical velocities are weak and vertical biomass fluxes are therefore gravitationally-  
494 driven ( $\langle w_s B \rangle > \langle wB \rangle$ ).

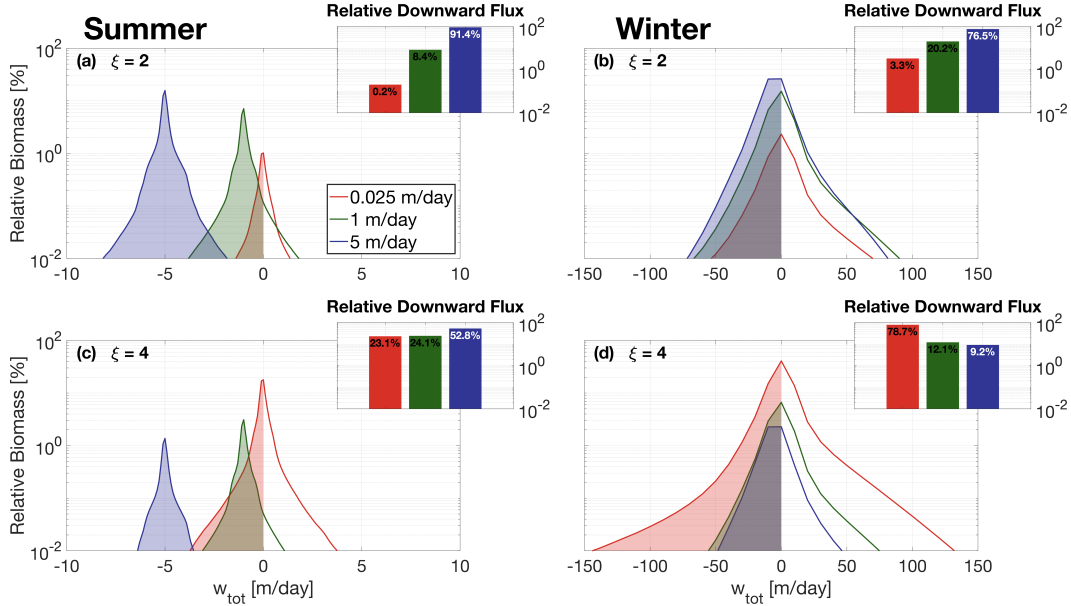
502 In the winter, PDFs of relative biomass as a function of vertical velocities present  
503 a much larger spread, with velocity magnitudes exceeding 50 m/day. For  $\xi = 2$ ,



457 **Figure 6.** [left] The median depth anomaly of particles with a sinking speed (a) 0.025 m/d,  
458 (b) 1 m/d, (c) 5 m/d within each grid cell for the winter case 25 days after particles are released.  
459 The ‘depth anomaly’ is with respect to the ‘expected’ sinking depth (= sinking speed  $\times$  time  
460 since release). Blue (red) grid cells indicate that the median depth of particles in this cell is  
461 deeper (shallower) than expected, based on a 1D gravitational model where  $z = w_s \times t$ . [right] (d)  
462 Probability Distribution Function (PDF) of particles as a function of depth for each velocity class  
463 (red = 0.025 m/day; green = 1 m/day; blue = 5 m/day). The winter distribution is shown as  
464 thick lines, while the summer distribution is represented by the shaded regions. Triangle markers  
465 indicate the expected depth of particles after 25 days based on the 1D gravitational model, which  
466 is used as a reference to compute the depth anomalies. Release depth is indicated by the thick  
467 dashed line.

504 the relative contribution of slower-sinking particles to the downward flux significantly  
505 increases from 0.2% in the summer to about 3% in the winter, demonstrating the  
506 impact advective velocities alone can have on vertical fluxes (Figure 7b). Nevertheless,  
507 slower-sinking particles remain a relatively small contributor to the total downward  
508 flux of biomass. When winter ocean dynamics are coupled with a steeper Junge slope,  
509 however, slower-sinking particles largely dominate the downward biomass flux. In  
510 our winter simulations with  $\xi = 4$ , we find that the slowest-sinking particle class is  
511 responsible for about 79% of the biomass flux (Figure 7d).

512 Our results show that both a steepening of the particle size spectrum and the  
513 presence of submesoscale dynamics can enhance the contribution of slower-sinking parti-  
514 cles to the downward biomass flux. While the former is simply due to an increase in  
515 particle density in slower-sinking particle classes, the latter is attributed to the larger  
516 vertical velocity generated by submesoscale instabilities. When both are combined,  
517 as expected in the wintertime, slower-sinking particles then become the leading con-  
518 tributor to the downward biomass transport. However, slower-sinking particles are  
519 generally expected to remineralize on timescales shorter than their export timescale,  
520 fueling the argument that the focus should be upon faster-sinking particle classes. The



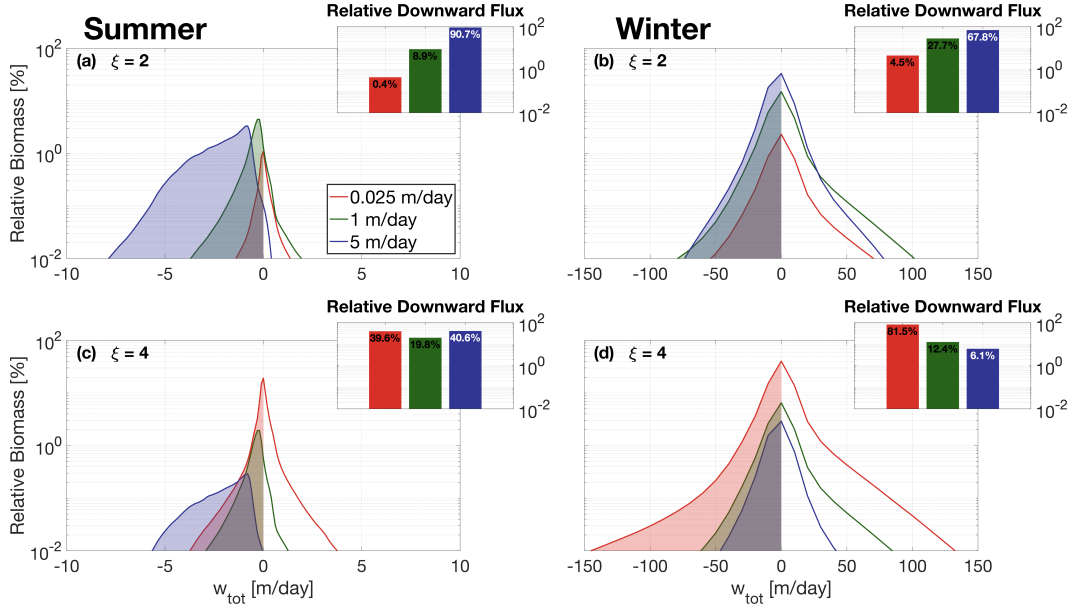
495 **Figure 7.** Probability Distribution Function (PDF) of relative biomass versus total vertical  
 496 velocity (sinking + advective) along particle trajectories in the summer case [left] and winter case  
 497 [right], with a Junge slope of 2 [top] and 4 [bottom]. PDFs are computed from the whole 24-day  
 498 particle tracking experiments. Inserts show the integrated relative downward biomass flux asso-  
 499 ciated with each sinking-velocity class, categorized according to their initial sinking velocity (red  
 500 = 0.025 m/day; green = 1 m/day; blue = 5 m/day). Both winter dynamics and steeper Junge  
 501 slopes tend to increase the relative contribution of slower-sinking particles.

521 impacts of remineralization on export are thus considered in the following section to  
 522 test the robustness of the findings.

### 523 3.3 Particle Remineralization

524 Both submesoscale dynamics and the Junge slope were identified as key factors  
 525 impacting the respective role played by different particle classes in driving downward  
 526 biomass fluxes. Simple Lagrangian particles were used to isolate the effects of these  
 527 two factors. In reality, however, sinking velocities of particulate matter varies in time  
 528 as the particles slowly remineralize. A remineralizing behavior was therefore imple-  
 529 mented for the Lagrangian particles, using Equation (10), to investigate the impact  
 530 that remineralization processes have on our findings. The traditional paradigm relies  
 531 on the fact that slow-sinking particles tend to fully remineralize over short timescales,  
 532 further enhancing the importance of faster-sinking particles classes in driving down-  
 533 ward biomass fluxes. While this paradigm holds for flatter Junge slope, where the  
 534 biomass content is dominated by faster-sinking particles, it becomes unfit at steeper  
 535 slopes.

536 Figure 8 compares the relative biomass and downward biomass fluxes associated  
 537 with each of the modeled particle classes for  $\xi = 2$  and  $\xi = 4$  including the remineral-  
 538 ization scheme. As previously detailed, downward fluxes of biomass are dominated by  
 539 faster-sinking particles during summertime and in the absence of remineralization (see  
 540 Figure 7). This is due to the fact that the flux of biomass  $\langle w_{tot}B \rangle = \langle w_s B \rangle + \langle w B \rangle$   
 541 is driven by  $\langle w_s B \rangle$ , despite a smaller relative biomass content per particle. This is  
 542 characteristic of a gravitationally-driven system, where settling velocity dictates the



548 **Figure 8.** Same as Figure 7, but including particle remineralization (see Equation 10).

543 contribution to downward fluxes. Implementing remineralization processes, however,  
 544 directly affects the particle settling velocity which slows down as particles remineralize.  
 545 This effect can particularly be seen in Figure 8a and c, where PDFs of relative biomass  
 546 per particle class are shifted towards weaker vertical velocities than in the absence of  
 547 remineralization, as predicted by Equation (10).

549 In an advectively-driven system where  $\langle w_s B \rangle \sim \langle w B \rangle$ , the relative amount of  
 550 biomass content in a particle class becomes important and dictates the respective con-  
 551 tribution of each particle class to the total downward biomass fluxes. This shift from a  
 552 gravitationally-driven to an advectively-driven system is observed when implementing  
 553 particle remineralization in the summer (Figure 8): in the absence of remineralization,  
 554 faster-sinking particles dominate the downward biomass fluxes (53%; see Figure 7c).  
 555 When remineralization processes are considered, slower-sinking particles contribute  
 556 more to biomass fluxes (see inset in Figure 8c). As shown in Figure 7, downward  
 557 biomass fluxes in the wintertime are generally advectively-driven, due to the larger  
 558 vertical velocities associated with wintertime ocean dynamics. Biomass fluxes are  
 559 dominated by the slower-sinking particles when  $\xi = 4$ , representing 79% of the down-  
 560 ward biomass flux (Figure 7d). Even after implementing the remineralization scheme,  
 561 slower-sinking particles remain the largest contributor to downward biomass fluxes  
 562 (82%; see Figure 8d).

563 These results highlight the importance in considering slower-sinking particle  
 564 classes when considering downward biomass fluxes. It also demonstrates that, con-  
 565 trarily to the traditional paradigm, remineralization processes enhance the role played  
 566 by slower-sinking particles in biomass fluxes, in cases where the biomass spectrum  
 567 slope is negative.

568 **4 Discussion**569 **4.1 Dynamical Regimes**

570 *Papa-summer* and *Papa-winter* experiments were designed to statistically capture  
 571 the ocean dynamics at Station Papa (145°W, 50°N) in the Northeast Pacific  
 572 Ocean. After spin-up, the model demonstrated similar distributions of both horizontal  
 573 ( $M^2$ ) and vertical ( $N^2$ ) density gradients to observational estimates from underwater  
 574 gliders (see Figures 2, 3, and 5). The two experiments, however, show significantly  
 575 different distributions of  $M^2$ , with the winter distribution exhibiting a longer tail, due  
 576 to sharper density gradients. The tail of the wintertime distribution is only partially  
 577 captured by the glider data, due to the fact that underwater gliders sampled gradients  
 578 at spatial scales of 10 km and greater, while the model has a horizontal resolution of  
 579 500 m, allowing sharper submesoscale fronts and filaments to be formed.

580 Studies investigating submesoscale dynamics traditionally focused on regions  
 581 where the presence of submesoscale fronts and filaments are established, such as west-  
 582 ern boundary currents with strong gradients (D'Asaro et al., 2011; Thomas, Tandon, &  
 583 Mahadevan, 2013), or the edge of mesoscale features (van Haren et al., 2006; Waite et  
 584 al., 2016). The seasonality in submesoscale dynamics captured in the glider dataset at  
 585 Station Papa and reflected in the model experiments, echoes the behavior seen from  
 586 recent observational studies conducted at a similar latitude in the Atlantic Ocean,  
 587 which demonstrate the intensification of submesoscale dynamics in the wintertime  
 588 (Thompson et al., 2016; Buckingham et al., 2016; Erickson & Thompson, 2018). De-  
 589 spite being sometimes qualified as an “eddy desert” with low kinetic energy (Chelton  
 590 et al., 2011), ocean characteristics in the eastern part of the Pacific subpolar gyre  
 591 suggest the presence of submesoscale features in the wintertime: strong density gradi-  
 592 ents, localized Rossby numbers of order 1, a balanced Richardson number  $Ri_b = \frac{f^2 N^2}{M^4}$   
 593 smaller than 1, a positively skewed distribution in vorticity, and a negatively skewed  
 594 distribution of vertical velocities (see Figure 5; Thomas, Taylor, et al., 2013; Rudnick,  
 595 2001; Buckingham et al., 2016).

596 Strong downward velocities are hypothesized to enhance POC export by advect-  
 597 ing slower-sinking particles out of the mixed layer. *Papa-winter* indeed exhibits vertical  
 598 velocities more than 20 times larger than in *Papa-summer*. The vertical currents in  
 599 *Papa-winter*, however, tend to be much patchier than the weaker vertical currents  
 600 observed in *Papa-summer*. Because both particle production and downward vertical  
 601 velocities present a high degree of patchiness, it requires a certain level of covariance  
 602 between the two fields for the export to effectively be enhanced (Mahadevan et al.,  
 603 2012). A more realistic seeding strategy for Lagrangian particles, such as one guided  
 604 by biological tracers, would likely provide important information towards a better  
 605 understanding of the effects of patchiness on POC export at submeso-scales

606 The hypothesis tested in this study is that submesoscale activity enhances export  
 607 of particulate matter at Station Papa by shortening the export timescale of particulate  
 608 matter. The wintertime intensification in submesoscale activity has the potential to  
 609 indeed enhance export (see discussion in Section 4.2). However, the seasonal cycle  
 610 in submesoscale activity is out of phase with the one in net community productivity,  
 611 which peaks in the spring and summertime when the mixed layer is shallower (Plant  
 612 et al., 2016). Two mechanisms are therefore present to potentially sustain a year-long  
 613 POC export flux: In the winter, less particulate material is present in the mixed layer,  
 614 but active submesoscale dynamics tend to enhance the POC export flux by advecting  
 615 the more numerous slower-sinking particles into the ocean interior. In the summer,  
 616 the production of POC is at its yearly maximum, but export tends to be dominated  
 617 by gravitational sinking, which favors faster-sinking particles and thus exclude part of  
 618 the particle spectrum from contributing to the export flux.

619            **4.2 Downward Fluxes**

620            Analyses of particle tracking experiments reveal that the contribution of slower-  
 621 sinking particles to the downward particulate flux depends on two main factors: (1)  
 622 the dynamics of the oceanic flow field, and (2) the slope of the size spectrum (i.e., the  
 623 Junge slope  $\xi$ ).

624            Mixed layer ocean dynamics at station Papa change significantly between the  
 625 winter and the summer. In the winter, submesoscale dynamics are intensified, and  
 626 sharp fronts and filaments develop in the mixed layer. This seasonal change in dy-  
 627 namics is consistent with recent observations (Thompson et al., 2016; Buckingham et  
 628 al., 2016), and models (Brannigan et al., 2015; Callies et al., 2015; Rocha et al., 2016)  
 629 characterizing the seasonal cycle of submesoscale dynamics. The winter intensification  
 630 in submesoscale dynamics was proven to have an important impact on the downward  
 631 flux of all sinking-velocity classes modeled in this experiment.

632            In the summer, gravitational sinking governs a downward particulate flux, which  
 633 is dominated by faster-sinking particles, with little to no contribution from slower-  
 634 sinking particles. In the winter, however, vertical fluxes tend to be advectively-driven,  
 635 which leads to a slightly weaker downward flux of faster-sinking particles than in the  
 636 summer due to resuspension, but a much larger flux of slower-sinking particles, which  
 637 are present in far greater numbers (Figure 7). The gravitationally-driven flux in the  
 638 summer is mechanistically different from the advectively-driven winter flux, which  
 639 raises the question as to which process is most efficient in driving a downward flux of  
 640 particulate material.

641            In the absence of remineralization, both a steeper size spectrum slope ( $\xi > 3$  in  
 642 this case) and enhanced submesoscale dynamics, increase the contribution of slower-  
 643 sinking particle classes to the downward biomass flux. This is only when both of  
 644 these conditions are combined, however, that slower-sinking particles dominate the  
 645 downward flux of biomass (Figure 7). This is a significant result, as Junge slopes  
 646 greater than 3 have been observed in the ocean: In-situ observations yield average  
 647 spectral slopes varying between 3.5 and 4.5 (see Table 2 in Kostadinov et al., 2009),  
 648 while spectral analysis of satellite data suggest global spectral slopes varying between  
 649 3 and 6. More recent observational work located in the Northeast Pacific, including  
 650 Station Papa, found a spectral slope also greater than 3 (White et al., 2015; Cram et  
 651 al., 2018). Junge slopes are expected to vary in space, depending on the community  
 652 composition, both lateraly and vertically (Kostadinov et al., 2009; White et al., 2015),  
 653 as well as in time; spectrum slopes tend to be flatter during a spring bloom event, where  
 654 larger particles (e.g., diatoms) are produced in large quantities, and steeper during the  
 655 wintertime, when communities are mostly composed of small particles (Parsons &  
 656 Lalli, 1988; Dale et al., 1999; Behrenfeld, 2010). The threshold value of  $\xi = 3$  for a  
 657 change in the biomass spectral slope (see Figure 4b) is of course a consequence of first-  
 658 order approximations used in this study describing the relationships between particle  
 659 size, sinking velocity, and biomass content. Nevertheless, our results demonstrate the  
 660 importance of including the smaller particle size range of the particle spectrum, in the  
 661 estimation or measurement of vertical fluxes, especially when submesoscale dynamics  
 662 are active. It also highlights the importance of better constraining the relationships  
 663 linking particle size, sinking velocity, and biomass content.

664            Introducing remineralization processes significantly decreases the biomass flux.  
 665 Counter-intuitively, however, the implementation of a remineralization scheme further  
 666 strengthens the contribution of slower-sinking particles to the biomass flux, once par-  
 667 ticles have left the euphotic layer (Figure 8). This can be explained by the fact that  
 668 remineralization processes have a greater impact on sinking-velocity classes that rely  
 669 on gravitational sinking to be exported, as these particles decelerate as they reminer-  
 670 alize. In the summer, all particle classes are similarly affected by remineralization,

as downward fluxes are gravitationally-driven. In the winter, however, slower-sinking particles are exported through advective processes. Their export timescale is barely affected by remineralization processes as it only depends on local ocean dynamics. Changing the remineralization timescale would therefore only affect the results in a gravitationally-driven flux: increasing the timescales (i.e. slower remineralization) would give more weight to the smaller classes, while decreasing the timescales (i.e. faster remineralization) would favor faster sinking particles to drive the downward flux. In an advectively-driven flux, however, all particles classes are equally affected by remineralization (i.e. lose 12% of their biomass per day). While this affects the total amount of biomass flux, it does not impact the respective contributions of the different particle classes to the downward biomass flux.

These results are robust to the range of sinking rates explored. If one considers a particle class with a sinking rate far exceeding the vertical advective velocity (e.g., 100 m/day; Turner, 2015), then the associated biomass flux can be estimated by relying on the traditional 1-D paradigm, assuming  $w_{tot} \approx w_s$ . Combining this approximation with Equation 8 shows that the slope of the biomass flux spectrum is positive for  $\xi < 5$ , in which case very fast-sinking particles would dominate vertical biomass fluxes. However, for  $\xi > 5$ , the slope of the biomass flux spectrum becomes negative as well, meaning that the biomass flux is always dominated by the slow-sinking particle classes, regardless of the ocean dynamical regime. While values of  $\xi > 5$  have been estimated by Kostadinov et al. (2009) using satellite data, in-situ estimated values of  $\xi$  tend to range between 2 and 4.5 (White et al., 2015; Cram et al., 2018).

<sup>c1</sup>Our findings add to a rapidly growing body of literature supporting the key role of an export pathway from the upper ocean to the interior driven by vertical ocean dynamic, and directly affecting particulate carbon. This pathway is often referred to as the "particle-injection pump" (Boyd et al., 2019)<sup>c2</sup>, or "subduction hot spots" (Levy et al., 2013; Omand et al., 2015; Resplandy et al., 2019), <sup>c3</sup> and is consistently identified as an important mechanism to POC export (Siegel et al., 2016; Stukel et al., 2017, 2018; Llort et al., 2018). <sup>c4</sup>Vertical mixing at submesoscales, in fact, was found to be equally important for the subduction of tracers from the mixed layer to the interior, and the obduction of tracers having a subsurface maximum (e.g., nutrients) (Taylor et al., 2020; Mahadevan, 2016). <sup>c5</sup>The importance of the seasonality in submesoscales dynamics highlighted in our process-oriented study supports recent findings obtained from high-resolution observations: both Erickson and Thompson (2018) and Bol et al. (2018)<sup>c6</sup> studied glider data to conclude that the winter intensification of submesoscale dynamics can generate a large downward export of POC. The third key component to our results, additionally to the roles of submesoscale dynamics and seasonality, is the contribution of smaller, slower-sinking POC to the export flux. The results presented in this work directly align with studies providing evidence that smaller particles contribute significantly to the POC flux (Baker et al., 2017; Riley et al., 2012; Bol et al., 2018; Taylor et al., 2020). <sup>c7</sup> The magnitude of the downward flux driven by slow-sinking particles, however, is still uncertain and was sometimes estimated to be largely compensated by an upward flux (Resplandy et al., 2019), <sup>c8</sup> indicating a possible dependence on data resolution. In our study, we piece together three key components to POC vertical fluxes to characterize limit cases where ocean conditions favor ei-

<sup>c1</sup> *Text added.*

<sup>c2</sup> *Text added.*

<sup>c3</sup> *Text added.*

<sup>c4</sup> *Text added.*

<sup>c5</sup> *Text added.*

<sup>c6</sup> *Text added.*

<sup>c7</sup> *Text added.*

<sup>c8</sup> *Text added.*

ther a gravitationally- or advectively-driven POC flux. We reached the conclusion<sup>c9</sup> that slow- and non-sinking particles<sup>c10</sup>, compared to the magnitude of vertical currents, should be considered when studying the downward flux of particulate matter in the upper ocean.<sup>c11</sup> Furthermore, the patchiness associated with both particle production and submesoscale features poses a real observational challenge to properly resolve vertical fluxes. Based on our findings, subsequent studies could focus on testing the impact of patchiness on vertical fluxes. In the wintertime, when size spectral slope is steep and submesoscale dynamics most active, vertical fluxes could be grossly underestimated depending on the level of co-occurrence between particle production and stronger vertical currents.

## 5 Conclusion

The main conclusions of this study are:

1. Ocean dynamics in the subpolar Northeast Pacific exhibit a seasonal cycle with low submesoscale activity in the summertime, and more submesoscale features present in the wintertime. Submesoscale dynamics generate larger, and asymmetric, vertical currents leading to a vertical biomass flux driven by advective processes, as opposed to gravitational sinking in the summertime.
2. Submesoscale dynamics generally enhance the downward particulate flux by increasing the contribution of slower-sinking particles to the total flux through advective transport. The slower-sinking particles are found to be significant for export, and can be even make the dominant contribution under certain conditions.
3. The contribution of slower-sinking particles to the downward biomass flux depends on the slope of the particle size spectra (i.e., the Junge Slope), that controls the relative number of particles per size class. Two cases emerge from this study:
  - (a) If the Junge slope is smaller than 3, larger particles contribute most to vertical biomass fluxes independently of flow dynamics, as there are no mechanisms capable of selectively advecting slower-sinking particles. The system is described as gravitationally-driven.
  - (b) If the Junge slope is greater than 3, as most commonly observed, ocean dynamics become key for determining which particle classes dominate the downward flux. As submesoscale dynamics become more active, ageostrophic circulations leading to larger vertical velocities develop. In these conditions, downward biomass fluxes are largely driven by the slower-sinking particle classes.
4. Remineralization processes below the euphotic depth logically reduce the amount of biomass flux. However, it unexpectedly enhances the role of slower-sinking particles, which are advectively transported. The impact of remineralization below the euphotic depth is greater on faster-sinking particles since it affects both the biomass content and their sinking velocity.

## Acknowledgments

The work was funded by NASA grant NNX16AR48G, to complement the EXport Processes in the global Ocean from RemoTe Sensing (EXPORTS) program. We would

<sup>c9</sup> The results of this study suggest

<sup>c10</sup> Text added.

<sup>c11</sup> Text added.

like to thank A. Thompson (Caltech) for his useful comments and suggestions, N. Pelland (NOAA) and C. Eriksen (University of Washington) for sharing the glider data collected at Ocean Station Papa, as well as S. Essink for his assistance in developing the particle-tracking code. All data used in this manuscript are publicly available: Ocean Station Papa data is available on PMEL's website (<https://www.pmel.noaa.gov/ocs/Papa>; PMEL, 2018) and gridded Argo products can be downloaded at <http://www.seanoe.org/data/00348/45945> (Gaillard, 2015). Glider data is archived at the University of Washington's Library (<http://hdl.handle.net/1773/41656>; Pelland, 2018). Both the code and dataset necessary to reproduce analysis and figures are publicly available(Dever, 2020b, 2020a). Finally, we are grateful to the two anonymous reviewers for their valuable comments and suggestions.

## References

- Alkire, M., D'Asaro, E., Lee, C., Perry, M., Gray, A., Cetinic, I., ... González-Posada, A. (2012). Estimates of net community production and export using high-resolution, Lagrangian measurements of O<sub>2</sub>, NO<sub>3</sub><sup>-</sup>, and POC through the evolution of a spring diatom bloom in the North Atlantic. *Deep-Sea Res. I*, 64, 157-174. doi: 10.1016/j.dsr.2012.01.012
- Armstrong, R. A., Lee, C., Hedges, J. I., Honjo, S., & Wakeham, S. G. (2001). A new, mechanistic model for organic carbon fluxes in the ocean based on the quantitative association of poc with ballast minerals. *Deep Sea Research Part II*, 49(1), 219-236. doi: 10.1016/S0967-0645(01)00101-1
- Bach, L. T., Riebesell, U., Sett, S., Febiri, S., Rzepka, P., & Schulz, K. G. (2012). An approach for particle sinking velocity measurements in the 3–400 μm size range and considerations on the effect of temperature on sinking rates. *Marine Biology*, 159(8), 1853–1864. doi: 10.1007/s00227-012-1945-2
- Baker, C. A., Henson, S. A., Cavan, E. L., Giering, S. L., Yool, A., Gehlen, M., ... Sanders, R. (2017). Slow-sinking particulate organic carbon in the atlantic ocean: Magnitude, flux, and potential controls. *Global Biogeochemical Cycles*, 31(7), 1051-1065. doi: 10.1002/2017GB005638
- Behrenfeld, M. J. (2010). Abandoning sverdrup's critical depth hypothesis on phytoplankton blooms. *Ecology*, 91(4), 977-989. doi: 10.1890/09-1207.1
- Bol, R., Henson, S. A., Rumyantseva, A., & Briggs, N. (2018). High-frequency variability of small-particle carbon export flux in the northeast atlantic. *Global Biogeochemical Cycles*, 32(12), 1803-1814. doi: <https://doi.org/10.1029/2018GB005963>
- Bower, A. S., & Rossby, T. (1989). Evidence of Cross-Frontal Exchange Processes in the Gulf Stream Based on Isopycnal RAFOS Float Data. *Journal of Physical Oceanography*, 19(9), 1177–1190. doi: 10.1175/1520-0485(1989)019<1177:EOCFEP>2.0.CO;2
- Boyd, P. W., Claustre, H., Levy, M., Siegel, D. A., & Weber, T. (2019). Multi-faceted particle pumps drive carbon sequestration in the ocean. *Nature*, 568(7752), 327–335. doi: 10.1038/s41586-019-1098-2
- Brannigan, L., Marshall, D. P., Naveira-Garabato, A., & George Nurser, A. (2015). The seasonal cycle of submesoscale flows. *Ocean Modelling*, 92, 69–84. doi: 10.1016/j.ocemod.2015.05.002
- Briggs, N., Perry, M. J., Cetinic, I., Lee, C., D'Asaro, E., Gray, A. M., & Rehm, E. (2011). High-resolution observations of aggregate flux during a sub-polar north atlantic spring bloom. *Deep Sea Research Part I: Oceanographic Research Papers*, 58(10), 1031 - 1039. doi: 10.1016/j.dsr.2011.07.007
- Buckingham, C. E., Naveira Garabato, A. C., Thompson, A. F., Brannigan, L., Lazar, A., Marshall, D. P., ... Belcher, S. E. (2016). Seasonality of submesoscale flows in the ocean surface boundary layer. *Geophysical Research Letters*, 43(5), 2118–2126. doi: 10.1002/2016GL068009

- Callies, J., Ferrari, R., Klymak, J. M., & Gula, J. (2015). Seasonality in submesoscale turbulence. *Nature communications*, 6, 6862. doi: 10.1038/ncomms7862
- Chelton, D. B., Schlax, M. G., & Samelson, R. M. (2011). Global observations of nonlinear mesoscale eddies. *Progress in Oceanography*, 91(2), 167–216. doi: 10.1016/j.pocean.2011.01.002
- Cram, J. A., Weber, T., Leung, S. W., McDonnell, A. M. P., Liang, J.-H., & Deutsch, C. (2018). The Role of Particle Size, Ballast, Temperature, and Oxygen in the Sinking Flux to the Deep Sea. *Global Biogeochemical Cycles*, 32(5), 858-876. doi: 10.1029/2017GB005710
- Dale, T., Rey, F., & Heimdal, B. R. (1999). Seasonal development of phytoplankton at a high latitude oceanic site. *Sarsia*, 84(5-6), 419-435. doi: 10.1080/00364827.1999.10807347
- D'Asaro, E., Lee, C., Rainville, L., Harcourt, R., & Thomas, L. (2011). Enhanced turbulence and energy dissipation at ocean fronts. *Science*, 332(6027), 318–322. doi: 10.1126/science.1201515
- Dever, M. (2020a). *Size-differentiated Export Flux in Different Dynamical Regimes in the Ocean: the data*. doi: <http://dx.doi.org/10.17632/tr9y4s2534.1>
- Dever, M. (2020b). *Size differentiated Export GBC analysis: Release 1*. doi: 10.5281/zenodo.3908126
- DeVries, T., Liang, J.-H., & Deutsch, C. (2014). A mechanistic particle flux model applied to the oceanic phosphorus cycle. *Biogeosciences*, 11(19), 5381-5398. doi: 10.5194/bg-11-5381-2014
- Döös, K., Kjellsson, J., & Jönsson, B. (2013). TRACMASS – A Lagrangian Trajectory Model. In *Preventive methods for coastal protection* (pp. 225–249). Heidelberg: Springer International Publishing. doi: 10.1007/978-3-319-00440-2\_7
- Ducklow, H. W., Steinberg, D. K., & Buesseler, K. O. (2001). Upper Ocean Carbon Export and the Biological Pump. *Oceanography*, 14. doi: <https://doi.org/10.5670/oceanog.2001.06>
- Erickson, Z. K., & Thompson, A. F. (2018). The Seasonality of Physically Driven Export at Submesoscales in the Northeast Atlantic Ocean. *Global Biogeochemical Cycles*, 32(8), 1144–1162. doi: 10.1029/2018GB005927
- Estapa, M. L., Siegel, D. A., Buesseler, K. O., Stanley, R. H. R., Lomas, M. W., & Nelson, N. B. (2015). Decoupling of net community and export production on submesoscales in the Sargasso Sea. *Global Biogeochemical Cycles*, 29(8), 1266–1282. doi: 10.1002/2014GB004913
- Falkowski, P. G., Barber, R. T., & Smetacek, V. (1998). Biogeochemical Controls and Feedbacks on Ocean Primary Production. *Science*, 281(5374), 200–206. doi: 10.1126/science.281.5374.200
- Fox-Kemper, B., Ferrari, R., & Hallberg, R. (2008). Parameterization of Mixed Layer Eddies. Part I: Theory and Diagnosis. *Journal of Physical Oceanography*, 38(6), 1145–1165. doi: 10.1175/2007JPO3792.1
- Gaillard, F. (2015). *ISAS-13 temperature and salinity gridded fields*. SEANOE. doi: 10.17882/45945
- Gaillard, F., Reynaud, T., Thierry, V., Kolodziejczyk, N., & von Schuckmann, K. (2016). In situ-based reanalysis of the global ocean temperature and salinity with isas: Variability of the heat content and steric height. *Journal of Climate*, 29(4), 1305-1323. doi: 10.1175/JCLI-D-15-0028.1
- Gruber, N., Lachkar, Z., Frenzel, H., Marchesiello, P., Münnich, M., McWilliams, J. C., ... Plattner, G.-K. (2011). Eddy-induced reduction of biological production in eastern boundary upwelling systems. *Nature geoscience*, 4(11), 787. doi: 10.1038/NGEO1273
- Harrison, P. J., Whitney, F. A., Tsuda, A., Saito, H., & Tadokoro, K. (2004). Nutrient and Plankton Dynamics in the NE and NW Gyres of the Subarctic Pacific Ocean. *Journal of Oceanography*, 60(1), 93–117. doi:

- 868 10.1023/B:JOCE.0000038321.57391.2a  
 869 Hoskins, B. J., & Bretherton, F. P. (1972). Atmospheric Frontogenesis Models:  
 870 Mathematical Formulation and Solution. *Journal of the Atmospheric Sciences*,  
 871 29(1), 11–37. doi: 10.1175/1520-0469(1972)029<0011:AFMMFA>2.0.CO;2  
 872 Iversen, M. H., & Ploug, H. (2010). Ballast minerals and the sinking carbon flux in  
 873 the ocean: carbon-specific respiration rates and sinking velocity of marine snow  
 874 aggregates. *Biogeosciences*, 7(9), 2613–2624. doi: 10.5194/bg-7-2613-2010  
 875 Iversen, M. H., & Ploug, H. (2013). Temperature effects on carbon-specific respi-  
 876 ration rate and sinking velocity of diatom aggregates - potential implications  
 877 for deep ocean export processes. *Biogeosciences*, 10(6), 4073–4085. doi:  
 878 10.5194/bg-10-4073-2013  
 879 Jackson, G. A., Maffione, R., Costello, D. K., Alldredge, A. L., Logan, B. E., &  
 880 Dam, H. G. (1997). Particle size spectra between 1  $\mu\text{m}$  and 1 cm at Monterey  
 881 Bay determined using multiple instruments. *Deep Sea Research Part I*, 44(11),  
 882 1739–1767. doi: 10.1016/S0967-0637(97)00029-0  
 883 Klein, P., & Lapeyre, G. (2009). The Oceanic Vertical Pump Induced by Mesoscale  
 884 and Submesoscale Turbulence. *Annual Review of Marine Science*, 1(1), 351–  
 885 375. doi: 10.1146/annurev.marine.010908.163704  
 886 Kostadinov, T. S., Siegel, D. A., & Maritorena, S. (2009). Retrieval of the particle  
 887 size distribution from satellite ocean color observations. *Journal of Geophysical  
 888 Research*, 114(C9), C09015. doi: 10.1029/2009JC005303  
 889 Levy, M., Bopp, L., Karleskind, P., Resplandy, L., Ethe, C., & Pinsard, F. (2013).  
 890 Physical pathways for carbon transfers between the surface mixed layer and  
 891 the ocean interior. *Global Biogeochemical Cycles*, 27(4), 1001–1012. doi:  
 892 <https://doi.org/10.1002/gbc.20092>  
 893 Lévy, M., Ferrari, R., Franks, P. J. S., Martin, A. P., & Rivière, P. (2012). Bringing  
 894 physics to life at the submesoscale. *Geophysical Research Letters*, 39(14), n/a–  
 895 n/a. doi: 10.1029/2012GL052756  
 896 Lévy, M., Klein, P., & Treguier, A.-M. (2001). Impact of sub-mesoscale physics on  
 897 production and subduction of phytoplankton in an oligotrophic regime. *Jour-  
 898 nal of marine research*, 59(4), 535–565. doi: 10.1357/002224001762842181  
 899 Llort, J., Langlais, C., Matear, R., Moreau, S., Lenton, A., & Strutton, P. G. (2018).  
 900 Evaluating Southern Ocean Carbon Eddy-Pump From Biogeochemical-Argo  
 901 Floats. *Journal of Geophysical Research: Oceans*, 123(2), 971–984. doi:  
 902 10.1002/2017JC012861  
 903 Mahadevan, A. (2016). The Impact of Submesoscale Physics on Primary Produc-  
 904 tivity of Plankton. *Annual Review of Marine Science*, 8(1), 161–184. doi: 10  
 905 .1146/annurev-marine-010814-015912  
 906 Mahadevan, A., & Archer, D. (2000). Modeling the impact of fronts and  
 907 mesoscale circulation on the nutrient supply and biogeochemistry of the up-  
 908 per ocean. *Journal of Geophysical Research: Oceans*, 105(C1), 1209–1225. doi:  
 909 10.1029/1999JC900216  
 910 Mahadevan, A., D'Asaro, E., Lee, C., & Perry, M. J. (2012). Eddy-Driven Strat-  
 911 ification Initiates North Atlantic Spring Phytoplankton Blooms. *Science*,  
 912 337(6090), 54–58. doi: 10.1126/science.1218740  
 913 Mahadevan, A., Olinger, J., & Street, R. (1996a). A Nonhydrostatic Mesoscale Ocean  
 914 Model. Part II: Numerical Implementation. *Journal of Physical Oceanography*,  
 915 26(9), 1881–1900. doi: 10.1175/1520-0485(1996)026<1881:ANMOMP>2.0.CO;  
 916 2  
 917 Mahadevan, A., Olinger, J., & Street, R. (1996b). A Nonhydrostatic mesoscale ocean  
 918 model. Part I: Well-posedness and scaling. *Journal of Physical Oceanography*,  
 919 26(9), 1868–1880. doi: 10.1175/1520-0485(1996)026<1868:ANMOMP>2.0.CO;  
 920 2  
 921 Mahadevan, A., & Tandon, A. (2006). An analysis of mechanisms for submesoscale  
 922 vertical motion at ocean fronts. *Ocean Modelling*, 14(3-4), 241–256. doi: 10

- 923 .1016/J.OCEMOD.2006.05.006
- 924 McCave, I. (1984). Size spectra and aggregation of suspended particles in the deep  
925 ocean. *Deep Sea Research Part I*, 31(4), 329–352. doi: 10.1016/0198-0149(84)  
926 90088-8
- 927 McDonnell, A., & Buesseler, K. (2012). A new method for the estimation of sinking  
928 particle fluxes from measurements of the particle size distribution, average  
929 sinking velocity, and carbon content. *Limnology and Oceanography: Methods*,  
930 10, 329–346. doi: 10.4319/lom.2012.10.329
- 931 McDonnell, A. M. P., & Buesseler, K. O. (2010). Variability in the average sinking  
932 velocity of marine particles. *Limnology and Oceanography*, 55(5), 2085–2096.  
933 doi: 10.4319/lo.2010.55.5.2085
- 934 McWilliams, J. C. (2016). Submesoscale currents in the ocean. *Proceedings of the  
935 Royal Society A: Mathematical, Physical and Engineering Science*, 472(2189).  
936 doi: 10.1098/rspa.2016.0117
- 937 Mensa, J. A., Garraffo, Z., Griffa, A., Özgökmen, T. M., Haza, A., & Veneziani, M.  
938 (2013). Seasonality of the submesoscale dynamics in the Gulf Stream region.  
939 *Ocean Dynamics*, 63(8), 923–941. doi: 10.1007/s10236-013-0633-1
- 940 Mesinger, F., DiMego, G., Kalnay, E., Mitchell, K., Shafran, P. C., Ebisuzaki, W.,  
941 ... Shi, W. (2006). North american regional reanalysis. *Bulletin of the Ameri-  
942 can Meteorological Society*, 87(3), 343–360. doi: 10.1175/BAMS-87-3-343
- 943 Omand, M. M., D'Asaro, E. A., Lee, C. M., Perry, M. J., Briggs, N., Cetini, I.,  
944 & Mahadevan, A. (2015). Eddy-driven subduction exports particulate or-  
945 ganic carbon from the spring bloom. *Science*, 348(6231), 222–225. doi:  
946 10.1126/science.1260062
- 947 Omand, M. M., Govindarajan, R., He, J., & Mahadevan, A. (2020). Sinking flux of  
948 particulate organic matter in the oceans: Sensitivity to particle characteristics.  
949 *Scientific reports*, 10(1), 1–16. doi: 10.1038/s41598-020-60424-5
- 950 Parsons, T. R., & Lalli, C. M. (1988). Comparative oceanic ecology of the plankton  
951 communities of the subarctic atlantic and pacific oceans. *Oceanography and  
952 Marine Biology Annual Review*, 26, 317–359.
- 953 Pelland, N. (2018). *Seaglider Surveys at Ocean Station Papa: Bin-Averaged Profiles,  
954 Currents, and Independent Oxygen Data*. Retrieved from <http://hdl.handle.net/1773/41656>
- 955 Pelland, N., Eriksen, C., & Cronin, M. (2016). Seaglider surveys at Ocean Station  
956 Papa: Circulation and watermass properties in a meander of the North Pa-  
957 cific Current. *Journal of Geophysical Research: Oceans*, 121, 6816–6846. doi:  
958 10.1002/2016JC011920
- 959 Petrik, C., Jackson, G., & Checkley, D. (2013). Aggregates and their distributions  
960 determined from LOPC observations made using an autonomous profiling  
961 float. *Deep Sea Research Part I*, 74, 64–81. doi: 10.1016/j.dsr.2012.12.009
- 962 Plant, J. N., Johnson, K. S., Sakamoto, C. M., Jannasch, H. W., Coletti, L. J.,  
963 Riser, S. C., & Swift, D. D. (2016). Net community production at Ocean Sta-  
964 tion Papa observed with nitrate and oxygen sensors on profiling floats. *Global  
965 Biogeochemical Cycles*, 30(6), 859–879. doi: 10.1002/2015GB005349
- 966 Ploug, H., Iversen, M. H., Koski, M., & Buitenhuis, E. T. (2008). Production,  
967 oxygen respiration rates, and sinking velocity of copepod fecal pellets: Direct  
968 measurements of ballasting by opal and calcite. *Limnology and Oceanography*,  
969 53(2), 469–476. doi: 10.4319/lo.2008.53.2.0469
- 970 PMEL. (2018). *Pacific Marine Environment Laboratory Ocean Climate Sta-  
971 tions Mooring Data*. Retrieved from [https://www.pmel.noaa.gov/ocs/  
972 data-overview](https://www.pmel.noaa.gov/ocs/data-overview)
- 973 Resplandy, L., Lévy, M., & McGillicuddy, D. J. (2019). Effects of Eddy-Driven  
974 Subduction on Ocean Biological Carbon Pump. *Global Biogeochemical Cycles*,  
975 33(8), 1071–1084. doi: 10.1029/2018GB006125
- 976 Richardson, T., & Jackson, G. (2007). Small phytoplankton and carbon export from

- the surface ocean. *Science*, *315*, 838-840. doi: 10.1126/science.1133471
- Riley, J., Sanders, R., Marsay, C., Le Moigne, F. A., Achterberg, E. P., & Poultton, A. J. (2012). The relative contribution of fast and slow sinking particles to ocean carbon export. *Global Biogeochemical Cycles*, *26*(1). doi: 10.1029/2011GB004085
- Rocha, C. B., Gille, S. T., Chereskin, T. K., & Menemenlis, D. (2016). Seasonality of submesoscale dynamics in the Kuroshio Extension. *Geophysical Research Letters*, *43*(21), 11,304–11,311. doi: 10.1002/2016GL071349
- Rudnick, D. L. (2001). On the skewness of vorticity in the upper ocean. *Geophysical Research Letters*, *28*(10), 2045–2048. doi: 10.1029/2000GL012265
- Sheldon, R., Prakash, A., & Sutcliffe, W., Jr. (1972). The size distribution of particles in the ocean. *Limnology and Oceanography*, *17*(3), 327-340. doi: 10.4319/lo.1972.17.3.0327
- Sherry, N. D., Boyd, P. W., Sugimoto, K., & Harrison, P. J. (1999). Seasonal and spatial patterns of heterotrophic bacterial production, respiration, and biomass in the subarctic NE Pacific. *Deep-Sea Research Part II: Topical Studies in Oceanography*, *46*(11-12), 2557–2578. doi: 10.1016/S0967-0645(99)00076-4
- Siegel, D. A., Buesseler, K. O., Behrenfeld, M. J., Benitez-Nelson, C. R., Boss, E., Brzezinski, M. A., ... Steinberg, D. K. (2016). Prediction of the export and fate of global ocean net primary production: The exports science plan. *Frontiers in Marine Science*, *3*, 22. doi: 10.3389/fmars.2016.00022
- Stukel, M. R., Aluwihare, L. I., Barbeau, K. A., Chekalyuk, A. M., Goericke, R., Miller, A. J., ... others (2017). Mesoscale ocean fronts enhance carbon export due to gravitational sinking and subduction. *Proceedings of the National Academy of Sciences*, *114*(6), 1252–1257. doi: 10.1073/pnas.1609435114
- Stukel, M. R., & Ducklow, H. W. (2017). Stirring Up the Biological Pump: Vertical Mixing and Carbon Export in the Southern Ocean. *Global Biogeochemical Cycles*, *31*(9), 1420–1434. doi: 10.1002/2017GB005652
- Stukel, M. R., Song, H., Goericke, R., & Miller, A. J. (2018). The role of subduction and gravitational sinking in particle export, carbon sequestration, and the remineralization length scale in the California Current Ecosystem. *Limnology and Oceanography*, *63*(1), 363–383. doi: 10.1002/lno.10636
- Taylor, J. R., Smith, K. M., & Vreugdenhil, C. A. (2020). The influence of submesoscales and vertical mixing on the export of sinking tracers in large-eddy simulations. *Journal of Physical Oceanography*, *50*(5), 1319-1339. doi: 10.1175/JPO-D-19-0267.1
- Thomas, L. N., Tandon, A., & Mahadevan, A. (2013). Submesoscale processes and dynamics. In *Ocean modeling in an eddying regime* (p. 17-38). American Geophysical Union (AGU). doi: 10.1029/177GM04
- Thomas, L. N., Taylor, J. R., Ferrari, R., & Joyce, T. M. (2013). Symmetric instability in the Gulf Stream. *Deep Sea Research Part II: Topical Studies in Oceanography*, *91*, 96–110. doi: 10.1016/j.dsr2.2013.02.025
- Thompson, A. F., Lazar, A., Buckingham, C., Naveira Garabato, A. C., Damerell, G. M., & Heywood, K. J. (2016). Open-Ocean Submesoscale Motions: A Full Seasonal Cycle of Mixed Layer Instabilities from Gliders. *Journal of Physical Oceanography*, *46*(4), 1285–1307. doi: 10.1175/JPO-D-15-0170.1
- Turner, J. T. (2015). Zooplankton fecal pellets, marine snow, phytodetritus and the ocean's biological pump. *Progress in Oceanography*, *130*, 205–248.
- van Haren, H., Millot, C., & Taupier-Letage, I. (2006). Fast deep sinking in Mediterranean eddies. *Geophysical Research Letters*, *33*(4), L04606. doi: 10.1029/2005GL025367
- Waite, A. M., Stemmann, L., Guidi, L., Calil, P. H. R., Hogg, A. M. C., Feng, M., ... Gorsky, G. (2016). The wineglass effect shapes particle export to the deep ocean in mesoscale eddies. *Geophysical Research Letters*, *43*(18), 9791–9800. doi: 10.1002/2015GL066463

- 1033 White, A. E., Letelier, R. M., Whitmire, A. L., Barone, B., Bidigare, R. R., Church,  
1034 M. J., & Karl, D. M. (2015). Phenology of particle size distributions  
1035 and primary productivity in the North Pacific subtropical gyre (Station  
1036 ALOHA). *Journal of Geophysical Research: Oceans*, 120(11), 7381–7399.  
1037 doi: 10.1002/2015JC010897